Solar Energy 236 (2022) 576–585

Contents lists available at ScienceDirect

Solar Energy

journal homepage: www.elsevier.com/locate/solener

Exploring a high-carrier-mobility black phosphorus/$MoSe_2$ heterostructure for high-efficiency thin film solar cells

Guoqing Wang [a,b], Zongmei Guo [a,b], Chen Chen [a,b], Weili Yu [c], Bo Xu [d,*], Bin Lin [a,b,*]

[a] School of Mechanical and Electrical Engineering, University of Electronic Science and Technology of China, Chengdu 611731, China
[b] Yangtze Delta Region Institute (Huzhou), University of Electronic Science and Technology of China, Huzhou 313001, China
[c] GPL Photonic Laboratory, State Key Laboratory of Applied Optics, Changchun Institute of Optics, Fine Mechanics and Physics, Chinese Academy of Science, Changchun 130033, China
[d] Department of Physics, Laboratory of Computational Materials Physics, Jiangxi Normal University, Nanchang 330022, China

ARTICLE INFO

Keywords:
Surface and interface engineering
$MoSe_2$
Black phosphorus
Thin film solar cells
Power conversion efficiency

ABSTRACT

Transition metal dichalcogenides (TMDCs) with self-passivated surfaces, suitable bandgaps and high optical-absorption coefficients are very promising for thin film solar cells, but seriously hindered by low carrier mobility. Herein, we propose interface-engineered two-dimensional van der Waals heterostructure composed of high-carrier-mobility black phosphorus (BP) layer and $MoSe_2$ layer, and demonstrate a new-type BP/$MoSe_2$ heterostructure thin film solar cell with high efficiency. The electronic structure and optical properties of both BP/$MoSe_2$ and BP/MoS_2 heterostructures are systematically investigated. Compared with BP/MoS_2 heterostructure, BP/$MoSe_2$ heterostructure shows enhanced photoelectric characteristics. Additionally, BP/$MoSe_2$ heterostructure has greater light absorption intensity as well as a wider absorption range, achieving a much higher power conversion efficiency of up to 23.04%. It is found that the built-in electric field at the interface of BP/$MoSe_2$ heterostructure accelerates the separation of electron-hole pairs. This work provides a feasible strategy for using the BP/$MoSe_2$ heterostructure for next-generation high-specific-power thin film solar cells.

1. Introduction

In order to meet the challenges posed by climate change, seeking clean and renewable energy to replace fossil fuel energy is an urgent task to build an environment-friendly and sustainable society. Among them, solar energy, as an inexhaustible and renewable resource, has attracted extensive attention. Currently, there is a shortage of photovoltaic materials with high photoelectric conversion efficiency, which is the biggest barrier to solar energy use(Chapin et al., 1954; Gallagher et al., 2007). First generation photovoltaic materials are crystallized silicon, which includes monocrystalline silicon and polycrystalline silicon(Ginley et al., 2008). Currently, it holds a dominant position in the solar cell market. Monocrystalline silicon shows a photoelectric conversion efficiency of up to 31%, but its high cost prevents its use in more further applications(Shockley and Queisser, 1961). Recently, cadmium-based low-cost materials have been developed as photovoltaic materials of the second generation(Mathew et al., 2012; Mathew et al., 2004). Cadmium, nevertheless, is a toxic metal that is detrimental to the environment, and its practical application is limited. Additionally, halide perovskite materials(Burschka et al., 2013; Hassan et al., 2021; Jeong et al., 2021; Kojima et al., 2009; Lee et al., 2012; Liu et al., 2013; Min et al., 2021; Stranks et al., 2013; Yoo et al., 2021) have been proposed as potential candidate materials for solar cells, but their disadvantages are that they decompose easily and are unstable in moist air. Furthermore, organic semiconductor materials are also considered as the ideal next-generation solar cells because of their low manufacturing cost and strong processability.(Burschka et al., 2013; Kong et al., 2021; Lee et al., 2012; Wohrle and Meissner, 1991) Nevertheless, the power conversion efficiency of organic solar cells is currently low and the service life is short, which needs further research and improvement by scientists. Therefore, it is important and urgent for solar cells to explore more suitable photovoltaic materials with environmentally-friendly, high durability and high efficiency.

The emergence of two-dimensional (2D) materials(Castellanos-Gomez et al., 2012; Fleurence et al., 2012; Kim et al., 2020; Shao et al., 2017; Wang et al., 2018), represented by graphene(Novoselov et al., 2004), offers unprecedented opportunities to surpass traditional three-dimensional materials in making the third generation of high-

* Corresponding authors at: School of Mechanical and Electrical Engineering, University of Electronic Science and Technology of China, Chengdu 611731, China.
E-mail address: bin@uestc.edu.cn (B. Lin).

https://doi.org/10.1016/j.solener.2022.03.008
Received 10 January 2022; Received in revised form 2 March 2022; Accepted 4 March 2022
Available online 20 March 2022

performance thin film solar cells and demonstrates unparalleled superiority. Among the many known 2D materials, atomically-thin transition metal dichalcogenides (TMDCs) are superior to others due to their direct band-gap, inherent elasticity and high transparency(Mak et al., 2013; Mak et al., 2012; Mak and Shan, 2016; Ugeda et al., 2014; Wang et al., 2012). In addition, preparation of TMDCs is relatively easy by methods such as hydrothermal deposition, electrodeposition and vapor deposition. Chen *et al.*(Chen et al., 2015) successfully prepared MoS_2/WS_2 heterostructure using the chemical vapor deposition method and started to study its photovoltaic effect. Immediately, Tsai *et al.*(Tsai et al., 2017) measured the power conversion efficiency (PCE) of MoS_2/WS_2 heterostructure to be 2.56 % under AM 1.5G illumination. On the basis of these work, Li *et al.*(Li et al., 2018) studied the heterojunction's optical properties composed of monolayer $MoSe_2$ and MoS_2 via density functional theory (DFT). It has a PCE of about 12%. Recently, Vikraman *et al.* (Vikraman et al., 2021) constructed the $MoSe_2/WS_2$ heterostructure in experiments using the chemophysical methodology, which provided a PCE of 9.92%. And then, Najafidehaghani *et al.*(Najafidehaghani et al., 2021) synthesized $WS_2/MoSe_2$ heterostructure by chemical vapor deposition and tested the photovoltaic properties of p-n junctions based on the composition of these two monolayers. The maximum carrier mobility of organic semiconductors and quantum-dot (QD) materials is about the order of 1–10 $cm^2/V{\cdot}s$(Han et al., 2016; Hetsch et al., 2013; Wehrenfennig et al., 2014). Moreover, carrier mobility values of 100–300 $cm^2/V{\cdot}s$ have been demonstrated for TMDC materials(Chen et al., 2017; Chuang et al., 2014; Radisavljevic et al., 2011), which are 1, 2, or even more orders of magnitude higher than that of organic semiconductors and QD materials. Although compared with organic semiconductors and QD materials, the carrier mobilities of TMDC materials are still quite high. However, compared with traditional solar cell materials such as silicon and cadmium-based materials, the PCE of TMDC is not high enough, owing to their low carrier mobility (Cai et al., 2014; Conan et al., 1984; Klaassen, 1992; Larentis et al., 2012; Podzorov et al., 2004; Radisavljevic et al., 2011; van der Marel et al., 2003). Generally, surface and interface engineering via stacking two different types of monolayers together, their excellent characteristics can complement each other, and has become the main trend of thin film solar cell design.

Atomically-thin black phosphorus (BP) as a donor is promising, due to its direct band-gap semiconductor and excellent carrier mobility (Li et al., 2014; Qiao et al., 2014). The BP/MoS_2 van der Waals (vdW) p-n heterostructure was prepared by Deng *et al.* (Deng et al., 2014) and employed as the gate-tunable p-n diode, showing a maximum photodetection responsivity of 418 mA/W at 633 nm illumination. Moreover, a PCE of ~18% was obtained by Dai *et al.* (Dai and Zeng, 2014) using the bilayer-BP/MoS_2 heterostructure, indicating an enhancement of optoelectronic properties of MoS_2 via the BP/MoS_2 heterostructure. In this article, a new 2D vdW heterostructure of monolayer-BP/MoSe2 was further built with enhanced carrier mobility via surface and interface engineering, and demonstrated a new-type $BP/MoSe_2$ heterostructure solar cell with high efficiency. The heterostructure facilitates photogenerated carriers separation by establishing interfacial contacts between various semiconductors. The PCE of ultra-thin solar cells can be further improved to reduce heat loss.

2. Experimental

All the computational simulations carried out in this study were performed using the Vienna *ab initio* simulation package (VASP) (Kresse and Furthmuller, 1996; Kresse and Furthmüller, 1996; Kresse and Hafner, 1994), which is derived from density functional theory (DFT) (Liechtenstein et al., 1995; Neuhauser et al., 2014). We characterized the interaction between atomic nuclei and valence electrons by using a method known as the projector augmented wave (PAW). Based on the generalized gradient approximation (GGA), this pseudopotential was derived from the exchange–correlation function of Perdew-Burke-Ernzerhof (PBE) (Blöchl, 1994; Perdew et al., 1996; Kresse and Joubert, 1999). Using the modified optB86b-vdW method, the van der Waals (vdW) interactions were described in order to better simulate the weak interactions between layers (Grimme, 2006; Grimme et al., 2010). In the Brillouin zone, the Monkhorst-Pack method(Monkhorst and Pack, 1976) was used to measure special *k*-points. Additionally, the Brillouin zone was represented in the numerical model by two *k*-meshes: $2 \times 5 \times 1$ and $5 \times 9 \times 1$, which were used for $BP/MoSe_2$ and BP/MoS_2 heterostructures in the geometry optimization as well as electronic structure calculation. There was a 500 eV cut-off energy for the plane wave function. Atoms in heterostructures were completely relaxed. Relaxation convergence was 1×10^{-5} eV/atom, and interaction force between atoms was less more than 0.01 eV/Å. The 20 Å vacuum area along the *z*-direction was set to avoid adjacent unit-cell interactions. Charge transfer between atoms or elements can be achieved using the Bader Charge analysis method(Henkelman et al., 2006). Phonon frequencies were calculated and structural stability checked using PHONOPY(Baroni et al., 2001; Togo and Tanaka, 2015). The VESTA software visualizes our static calculations(Momma and Izumi, 2008).

The dielectric function usually describes the material's optical properties in the linear response range:

$$\varepsilon = \varepsilon_1(\omega) + i\varepsilon_2(\omega) \tag{1}$$

where ω is the photon frequency. The imaginary part $\varepsilon_2(\omega)$ of the dielectric function can be calculated directly from the electronic structure, which is closely related to the electronic response and can be expressed as(Gajdoš et al., 2006):

$$\varepsilon_2(\omega) = \frac{2e^2\pi}{\Omega\varepsilon_0}\sum_{k,c,v}\left|\left\langle\psi_k^c|\boldsymbol{u}\bullet\boldsymbol{r}|\psi_k^v\right\rangle\right|^2\bullet\delta(E_k^c - E_k^v - \hbar\omega) \tag{2}$$

here Ω is primitive cell volume. $\boldsymbol{k}$ is reciprocal vector. c is conduction band (CB) and v is valence band (VB). $\boldsymbol{u}$ is polarization direction vector of the incident electric field. E_k^c and E_k^v are energy of CB and VB. $\left|\left\langle\psi_k^c|\boldsymbol{u}\bullet\boldsymbol{r}|\psi_k^v\right\rangle\right|^2$ is momentum transition matrix element. $\hbar$ is reduced Planck constant. Additionally, the real part $\varepsilon_1(\omega)$ of the complex dielectric constant can be obtained from the imaginary part according to the Kramers-Kronig dispersion relationship(Toll, 1956):

$$\varepsilon_1(\omega) = 1 + \frac{2}{\pi}M\int_0^\infty \frac{\omega'\varepsilon_2(\omega)}{\omega'^2 - \omega^2}d\omega \tag{3}$$

where M is the principal value of integral. After obtaining the ε_1 and ε_2, the light absorption coefficient of the material can be expressed as(Wang et al., 2014):

$$\alpha(x) = \sqrt{2}\omega\left[\sqrt{\varepsilon_1^2(\omega) + \varepsilon_2^2(\omega)} - \varepsilon_1(\omega)\right]^{\frac{1}{2}} \tag{4}$$

Because of absorption, the intensity of light decays with depth x in material:

$$J(x) = J_0(1 - R)e^{-\alpha x} \tag{5}$$

where J_0, R, and α are incident light intensity, reflection coefficient, and normalized absorption coefficient, respectively. Hindrance coefficient $T(x)$ is measure of the incident light's stopping power:

$$T(x) = 1 - \frac{J(x)}{J_0} \tag{6}$$

here x is material thickness, and $\frac{J(x)}{J_0}$ is light transmittance in material.

3. Results and discussion

3.1. Construction of $BP/MoSe_2$ and BP/MoS_2 heterostructures

The primitive cells of the intrinsic $MoSe_2$ and MoS_2 monolayers are

hexagonal system (Figure S1). In contrast, the intrinsic black phosphorus (BP) monolayer belongs to cubic system. The BP/$MoSe_2$ and BP/MoS_2 heterostructures with BP were fabricated by modifying the lattice structures of $MoSe_2$ and MoS_2 to form the cubic system. Fig. 1 illustrates the primitive cell structures of $MoSe_2$, MoS_2, and BP monolayers. In Table 1, we present information about the lattice parameters and energy band structures of $MoSe_2$, MoS_2, and BP. In $MoSe_2$ monolayer, $a = 5.76$ Å & $b = 3.32$ Å are the optimized lattice parameters, and the Mo-Se bond length is 2.54 Å. It has a band-gap of 1.44 eV and is a direct band-gap semiconductor in which both conduction band minimum (CBM) and band maximum (VBM) are located at the *K* point. In MoS_2, optimized lattice parameters are $a = 5.53$ Å & $b = 3.20$ Å, and the Mo-S bond length is 2.42 Å. The MoS_2 monolayer is a direct band-gap semiconductor with a 1.61 eV band-gap. Among them, the CBM is at *K* point and the VBM is at *G* point. The lattice constants for the BP monolayer are $a = 4.39$ Å & $b = 3.37$ Å, and the P-P bond length is 2.24 Å. Similar to $MoSe_2$ and MoS_2 monolayer, BP is also a direct band-gap semiconductor. It has a 0.76 eV band-gap, as well as, both the CBM and VBM are at the *G* point. The total density of states (TDOS) of $MoSe_2$, MoS_2, and BP monolayers with cubic lattice are shown in Fig. 1b, d and f, respectively. Figure S2 shows the TDOS and band structure of $MoSe_2$ and MoS_2 monolayers with hexagonal lattice, as well as, the lattice parameters for them are listed in Table S1. The band structure of $MoSe_2$, MoS_2, and BP monolayers with cubic lattice and their phonon dispersion are exhibited in Figure S3. According to the above data, the method used is accurate and reliable based on theoretical(Cakir et al., 2014; Rawat et al., 2018; Souza et al., 2018; Wu et al., 2012) and experimental(Li et al., 2014; Wilson and Yoffe, 1969) results.

Using BP/$MoSe_2$ heterostructure as an example, it is assumed that this configuration is built directly from $MoSe_2$ and BP primitive cells.

Table 1
The lattice constants (a and b), angle (α), mismatch (δ), average interlayer distances (d_0), alignment type, and band-gap (E_g) in $MoSe_2$, MoS_2, BP monolayers, BP/$MoSe_2$ and BP/MoS_2 heterostructures.

	a (Å)	b (Å)	α (°)	δ (%)	d_0 (Å)	type	E_g (eV)
$MoSe_2$	5.76	3.32	90	–	–	–	1.44
MoS_2	5.53	3.20	90	–	–	–	1.61
BP	4.39	3.37	90	–	–	–	0.76
BP/$MoSe_2$	17.26	3.31	90	0.12	3.32	type-II	0.85
BP/MoS_2	17.26	3.31	90	4.04	3.28	type-II	0.05

According to $\delta = \frac{2|A-B|}{A+B} \times 100\%$, the lattice mismatch δ calculated in this case is up to 26.99% since their lattice constants are different along the *a*-axis. Here, A and B are the *x*-direction lattice constants for the $MoSe_2$/MoS_2, and BP primitive cell lattices, respectively. Moreover, $MoSe_2$ and BP monolayers have very little difference in *b*-axis, so δ = 1.49% in *y*-direction. The BP/$MoSe_2$ and BP/MoS_2 heterostructures should be constructed with better lattice matching. Accordingly, 4 × 1 × 1 BP was stacked on top of 3 × 1 × 1 $MoSe_2$ or MoS_2 to construct the heterostructures. Configurations of BP/$MoSe_2$ and BP/MoS_2 heterostructures are described in Fig. 2. After the optimization of the two heterostructures, BP/$MoSe_2$ and BP/MoS_2 have lattice parameters of a = 17.26 Å and b = 3.31 Å. In *x*-direction, the δ of BP/$MoSe_2$ heterostructure is only 0.12%, and BP/MoS_2 heterostructure's δ is 4.04%, which are all less than 5%(Kresse and Furthmuller, 1996). From this, it can be shown that BP/$MoSe_2$ and BP/MoS_2 heterostructures can be experimentally fabricated. It consists of 16 P atoms, 6 Mo atoms, 12 Se or 12 S atoms, totaling 34 atoms in the BP/$MoSe_2$ or BP/MoS_2 heterostructures. Fig. 2a and b are the optimized structures of heterostructures, with lattice constants of a = 17.26 Å & b = 3.31 Å, respectively. The

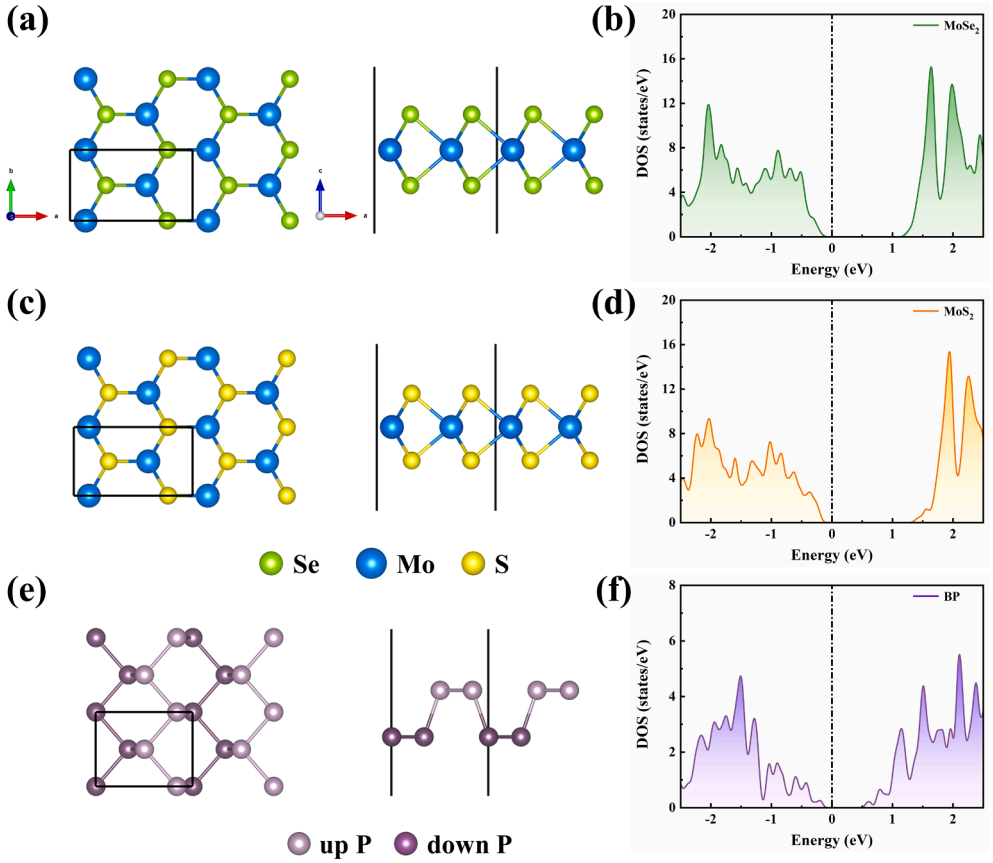

Fig. 1. Top (left) and side (right) views of (a) $MoSe_2$, (c) MoS_2, and (e) BP monolayers in cubic lattice. (b), (d), and (f) are the density of states (DOS) of $MoSe_2$, MoS_2, and BP monolayers, respectively. Green, blue, yellow, and purple balls represent S, Mo, Se, and P atoms. (For interpretation of the references to colour in this figure legend, the reader is referred to the web version of this article.)

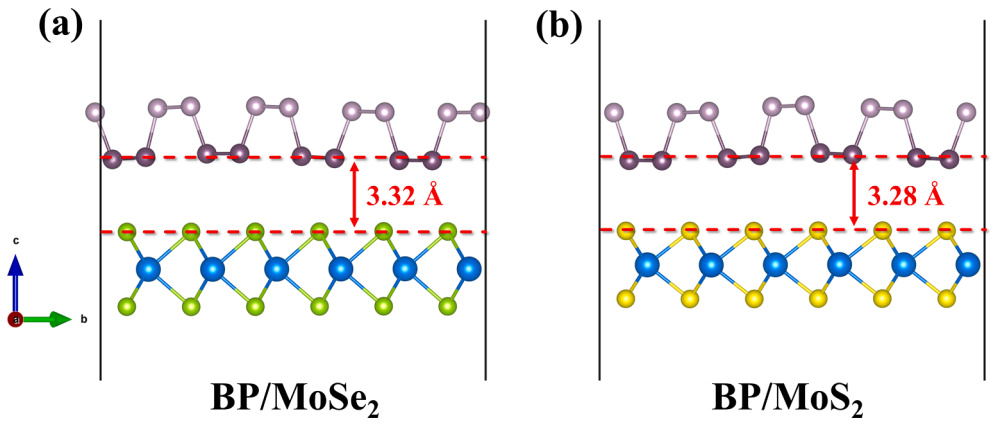

Fig. 2. The side view along the *a*-axis of (a) BP/$MoSe_2$ and (b) BP/MoS_2 heterostructures after optimized, respectively. The interlayer distances between the $MoSe_2$/MoS_2 and the BP layers are indicated by the distance between red dotted lines. (For interpretation of the references to colour in this figure legend, the reader is referred to the web version of this article.)

average interlayer distance for heterostructures can be obtained by averaging the coordinates of down-P atoms in BP layer and up-Se/up-S atoms in $MoSe_2$/MoS_2 layer. Each hetero-configuration has an average interlayer distance of 3.32 Å and 3.28 Å, respectively.

3.2. Electronic structures of BP/$MoSe_2$ and BP/MoS_2 heterostructures

To research the interfacial properties of 2D vdW heterostructures, an understanding of the electronic energy band structure is crucial. We further investigated the electronic properties of BP/$MoSe_2$ and BP/MoS_2 heterostructures after after verifying their structural details. A TDOS plot and weighted band structures are shown in Fig. 3 for BP/$MoSe_2$ and BP/MoS_2, respectively. In Fig. 3a, we can see that near Fermi-energy, the $MoSe_2$ layer contributes most to the TDOS in the conduction band (CB) of the BP/$MoSe_2$ heterostructure, while the BP layer contributes more to the TDOS at the valence band (VB). The green/yellow line and purple bubble in Fig. 3c and d depict the projected electron weight in the $MoSe_2$/MoS_2 layer and BP layer, respectively. In Fig. 3c and e, the VBM is primarily derived from the BP layer and the CBM originates primarily from the $MoSe_2$ layer, demonstrating an obvious formation of type-II band alignment in the BP/$MoSe_2$ heterostructure. In addition, the VBM and CBM are placed at the *G* point and near the *Y* point, respectively. As for the indirect band-gap, it is 0.85 eV. And besides, the calculated band-gap is 1.33 eV using the HSE06 method (Figure S4a). Hence, the BP/$MoSe_2$ heterostructure exhibits different electronic properties from intrinsic $MoSe_2$ and BP monolayers. The BP/MoS_2 heterostructure exhibits similar results to BP/$MoSe_2$. In Fig. 3b and d, the VBM is mostly provided by the BP layer, while the CBM primarily comes from the MoS_2, with an indirect band-gap amounts to approximately 0.05 eV. By using the HSE06 method, the band-gap is 0.72 eV (Figure S4b). The VBM and CBM are located at the *G* point and *Y*-*G* area, respectively, demonstrating a same type-II band alignment in the BP/MoS_2 heterostructure, as shown in Fig. 3d and f.

In an ideal solar cell system, the power conversion efficiency depends on the band-gap of material and the solar spectrum. When the solar spectrum is determined, the power conversion efficiency can be expressed as a function of the band-gap, which requires that the band-gap of the material has an appropriate value. As we know, the best band-gap is 1.34 eV, producing the maximum efficiency (Polman et al., 2016). However, if the band-gap is too small, the carrier kinetic energy generated by the battery when absorbing photons with higher energy is very large. In this case, carriers easily interact with the lattice, transferring the energy to the lattice vibration, and eventually loses it in the form of heat. Additionally, if the band-gap is too large, it is difficult for electrons to make transitions, and the short-circuit current density and optimum current density of the solar cell will be small, resulting in low power conversion efficiency(Nelson, 2003). In summary, the band-gap of BP/$MoSe_2$ heterostructure is closer to 1.34 eV, so it has the potential to be used as a thin film solar cell material.

3.3. Charge and electrostatic potential of BP/$MoSe_2$ and BP/MoS_2 heterostructures

Table 2 lists the charge gain or loss value of BP/$MoSe_2$ and BP/MoS_2 heterostructures. In BP/$MoSe_2$ heterostructure, the $MoSe_2$ loses 0.032 *e*, and the BP accumulates 0.032 *e*. Obviously, $MoSe_2$ is positively and BP is negatively charged, forming an electric field from $MoSe_2$ to BP. In BP/MoS_2 heterostructure, the BP loses 0.048 *e* and the MoS_2 gains 0.048 *e*. Intuitively, the electric field is shown to be pointing from BP to MoS_2 inside the interface. There will be an electric field in the heterogeneous structure because of charge transfer at the interface. The potential difference will exist between the two different layers if they are raised in potential and lowered in potential, respectively. Correspondingly, electrons fall in the negative forces that raise the potential energy, emerging an electric-field directional movement. So, there is a same direction for potential energy and electric field. The internal charge distribution of intrinsic $MoSe_2$ and MoS_2 monolayers is listed in Table S2.

Table 3 summarizes the work function (Φ), potential difference of $MoSe_2$/MoS_2 and BP layers (ΔΦ) as well as dipole moment (μ) of BP/$MoSe_2$ and BP/MoS_2 heterostructures. When the BP/$MoSe_2$ heterostructures are formed, $MoSe_2$ layer's potential decreases but layer's increases, and indicates that the charge is transferred from the $MoSe_2$ to the BP, as shown in Fig. 4a. Across two materials, the electrostatic potential difference ΔΦ is 0.41 eV. On the other hand, in the BP/MoS_2 heterostructure, MoS_2 potential increases while BP potential decreases. As a result, from BP to MoS_2, an interfacial electric field has been generated. In Fig. 4b, the electrostatic potential difference ΔΦ is 1.06. As discussed above, the data are in agreement with Bader Charge analysis. Dipole moments show that the μ of BP/$MoSe_2$ is 1.73 Debye and the μ of BP/MoS_2 is 1.28 Debye, demonstrating high electric field in BP/$MoSe_2$ heterostructure. Figure S5 shows the electrostatic potential of intrinsic $MoSe_2$ and MoS_2 monolayers.

We utilized the charge density difference in Fig. 4c and d to visualize the charge redistribution in the BP/$MoSe_2$ and BP/MoS_2 heterostructures as well as to understand the mechanism of charge-transfer. The difference in charge density between BP/$MoSe_2$ and BP/MoS_2 heterostructures has been performed using the following formula:

$$\Delta\rho(z) = \int \rho_{hetero}(x,y,z)dxdy - \int \rho_{MoSe2/MoS2}(x,y,z)dxdy - \int \rho_{BP}(x,y,z)dxdy \quad (7)$$

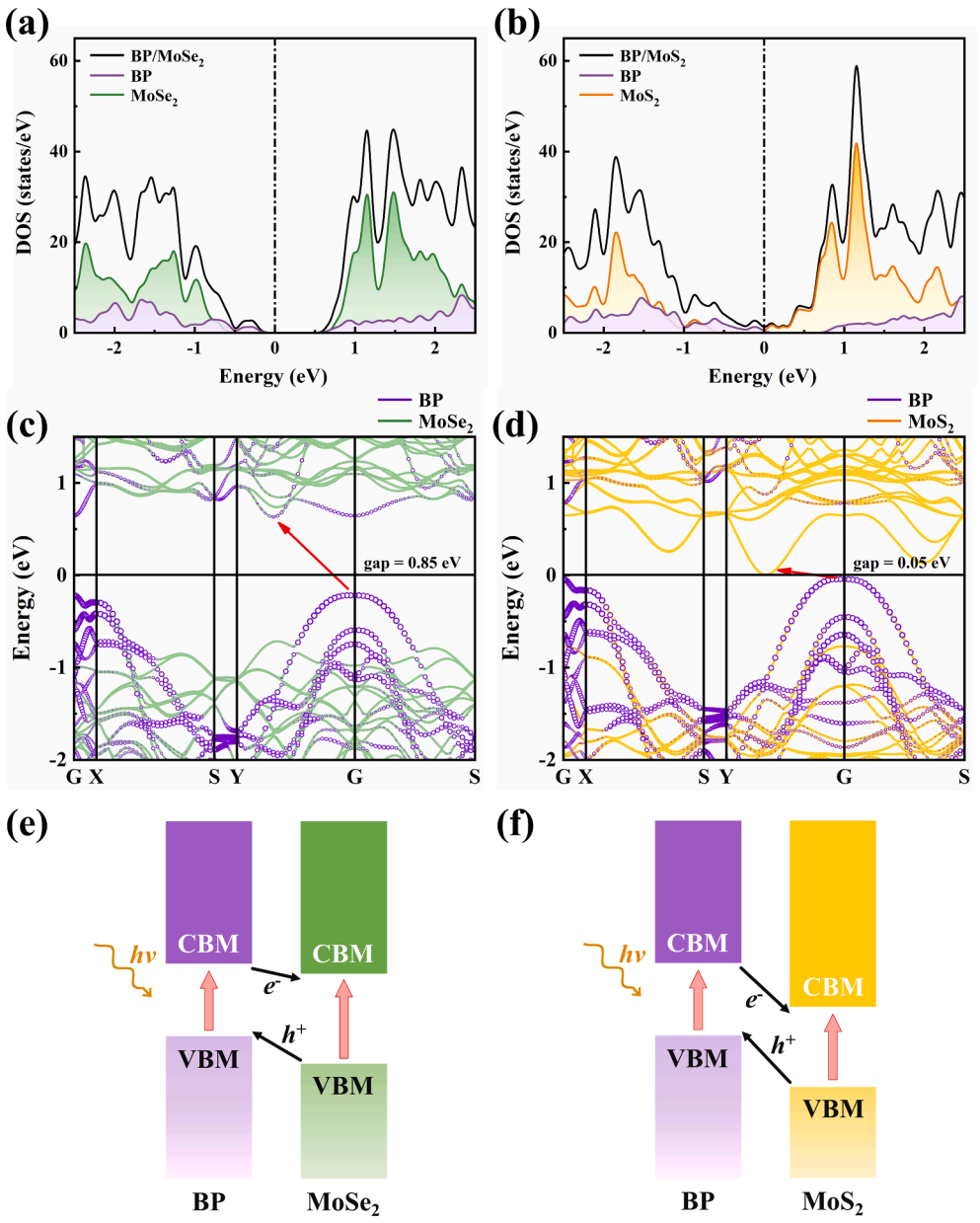

Fig. 3. The total density of states of (a) BP/$MoSe_2$ heterostructure and (b) BP/MoS_2 heterostructure. The projected band structure of (c) BP/$MoSe_2$ heterostructure and (d) BP/MoS_2 heterostructure. The type-II band alignment of (e) BP/$MoSe_2$ heterostructure and (f) BP/MoS_2 heterostructure.

Table 2
Charge gains and losses for P, Mo, S, and Se atoms on average. Σ_P, Σ_{MoSe2} and Σ_{MoS2} are gains or losses in total charges with BP, $MoSe_2$, and MoS_2 layers, respectively. (unit: *e*).

case	P_{up}	P_{down}	Σ_P	Mo	Se/S	$\Sigma_{MoSe2}/\Sigma_{MoS2}$
BP/$MoSe_2$	0.007	−0.003	0.032	−0.925	0.460	−0.032
BP/MoS_2	0.005	−0.011	−0.048	−1.214	0.611	0.048

Table 3
Work function (Φ), potential differences (ΔΦ), and dipole moment (μ) of BP/$MoSe_2$ and BP/MoS_2 heterostructures.

case	Φ (eV)	ΔΦ (eV)	μ (Debye)
BP/$MoSe_2$	5.47	0.41	1.73
BP/MoS_2	5.80	1.06	1.28

where $\rho_{hetero}(x,y,z)$,$\rho_{MoSe2/MoS2}(x,y,z)$, and $\rho_{BP}(x,y,z)$ are charge densities in heterostructure, $MoSe_2$/MoS_2 monolayer, and BP monolayer at the (x, y, z) point, respectively. It is seen in the inset that the charge density difference is represented by the corresponding isosurfaces. The blue and yellow areas are representative of the electron accumulations and depletions, respectively. In addition, the $MoSe_2$/MoS_2 layer and BP layer are demonstrated to undergo charge transfer via the interlayer, further suggesting that they have a built-in electric field (see the illustration in Fig. 4c and d for the schematic diagram). Fig. 4e and f display the electron localization functions (ELF), which depict real-space electron distributions. Due to their small charge transfer values, BP/$MoSe_2$ and BP/MoS_2 heterostructures exhibited essentially the same degree of charge aggregation compared to that of intrinsic $MoSe_2$ and MoS_2 monolayers (Figure S6).

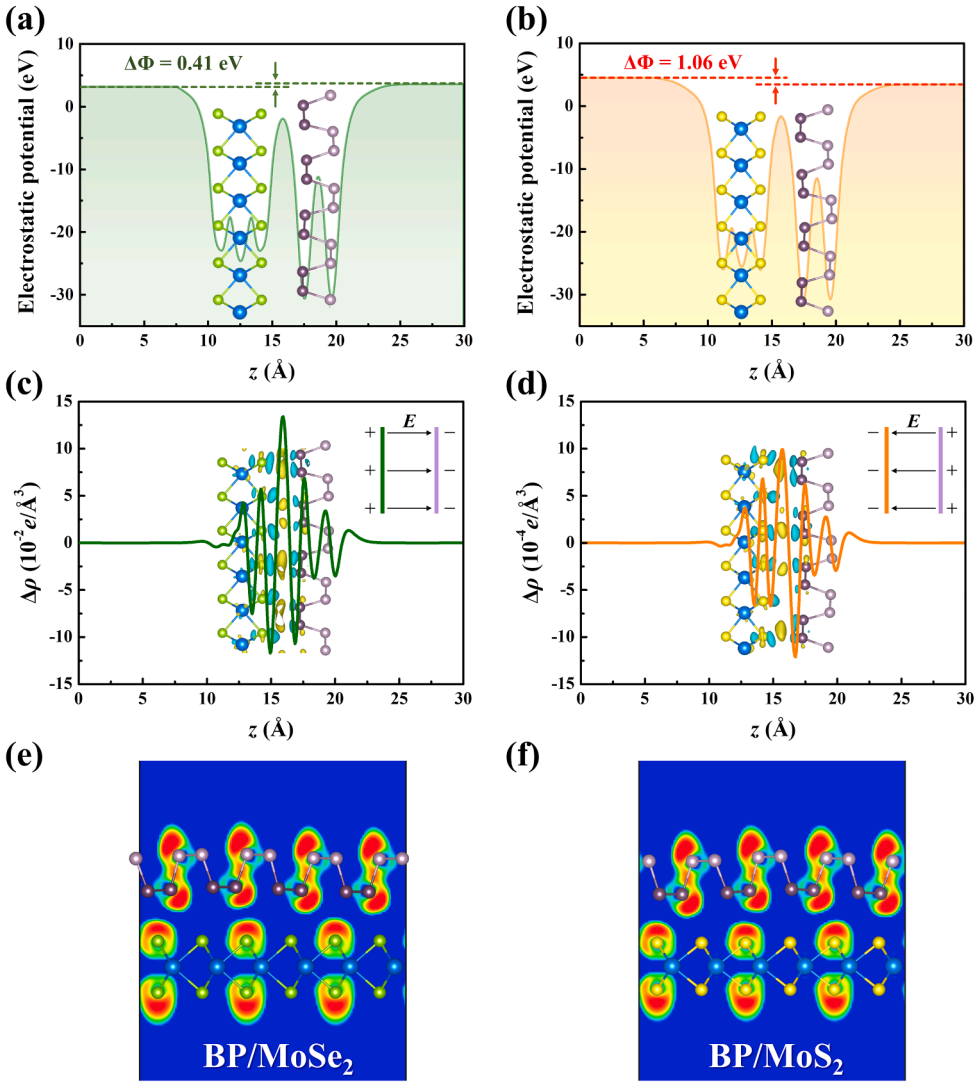

Fig. 4. The electrostatic potentials of (a) BP/$MoSe_2$ and (b) BP/MoS_2 heterostructures. (c) and (d) are the plane-averaged charge density difference. (e) and (f) are the ELF map on (0 1 0) crystal face.

3.4. Photoelectrical properties of BP/$MoSe_2$ and BP/MoS_2 heterostructures

Essentially, the dielectric constant ε represents the dielectric's response to an external electric field, which represents the dielectric's polarization degree under the external electric field. As a rule, the higher a material's dielectric constant is, the more polarization it can achieve. To deeply understand the differences between BP/$MoSe_2$ and BP/MoS_2 heterostructures in optical properties, the dielectric function was discussed and shown in Fig. 5a and b. At an energy of 0 eV, the real part ε_1's value of dielectric constant is the static permittivity. BP/$MoSe_2$ and BP/MoS_2 heterostructures have static permittivity of 13.55 and 5.50, respectively, as shown in Fig. 5a. The BP/$MoSe_2$ heterostructure, with a larger static permittivity, has a higher polarizability and a more intense photogenerated electric field than BP/MoS_2. Charges can be bound more efficiently in this system. Consequently, electron-hole pairs can be separated successfully and have a long lifetime in the BP/$MoSe_2$ heterostructure.

A dielectric function is characterized by the imaginary part ε_2 which measures the energy required to form the electric dipole. The ε_2 represents the interband-transition of the material as well as describes the degree of electron stimulated-transition. If ε_2 is larger, more likely it is that the electron will absorb photons. Generally, as the number of electrons in an excited state increases, the greater the probability of them transitioning. In comparison to BP/MoS_2, the ε_2 of BP/$MoSe_2$ has a low level of energy and a high peak, demonstrating an easier electron transition in the BP/$MoSe_2$ heterostructure.

Both BP/$MoSe_2$ and BP/MoS_2 heterostructures exhibit an optical absorption spectrum through theoretical calculation, as shown in Fig. 5c. Among them, spectrum of infrared region is 0–1.63 eV in energy range, visible light is 1.63–3.11 eV, and ultraviolet region is 3.11–6 eV. In the solar spectrum, visible light makes up 48.3%, infrared makes up 43% and ultraviolet makes up 8.7%. A comparison with BP/MoS_2 clearly demonstrates that the BP/$MoSe_2$ heterostructure exhibits a broader light range and superior light response characteristics across the full spectrum. Correspondingly, the BP/$MoSe_2$ heterostructure achieves an enhanced light absorption with a wider light response range. And besides, taking the BP/$MoSe_2$ heterostructure as an example, its absorption coefficient in the range of infrared and visible light is on the order of 1×10^5 cm^{-1}. Compared to several common solar cell materials (A. Luque, 2011; Greenaway, 1968; Nelson, 2003), such as, Ge (1×10^4 cm^{-1} to 5×10^5 cm^{-1}), InP (1×10^4 cm^{-1} to 5×10^5 cm^{-1}), GaAs (1×10^4 cm^{-1} to 1×10^5 cm^{-1}), c-Si (1×10^3 cm^{-1} to 0.5×10^5 cm^{-1}), and so forth, the absorption coefficient of BP/$MoSe_2$ heterostructure in this work is similar to that of these solar cell materials, which shows that BP/$MoSe_2$ as solar cell material can appropriate light absorption intensity

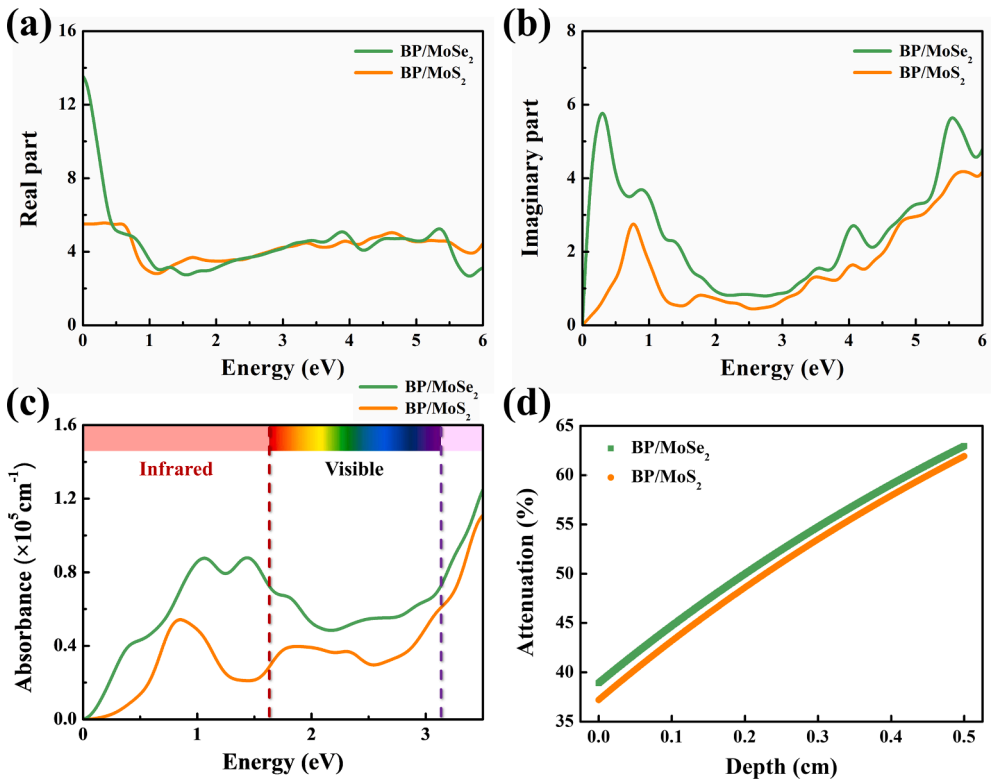

Fig. 5. (a) Real part of dielectric function for heterostructures. (b) Imaginary part of dielectric function. (c) Absorption spectra. (d) Hindrance coefficient map.

and exhibit the high performance similarly. Figure S7 shows the optical properties of heterostructures from 0–20 eV.

The light hindrance coefficient diagram can be seen in Fig. 5d. Material transmittance is determined by the hindrance coefficient. Materials' light absorption levels are proportional to the reciprocal value of the transmittance. $BP/MoSe_2$ and BP/MoS_2 heterostructures have hindrance coefficients of 38.9% and 37.2%, respectively. Thus, the transmittance $\frac{J(x)}{J_0}$ is 61.1% and 62.8%. According to equation $A = \lg(\frac{1}{\frac{J(x)}{J_0}})$, $BP/MoSe_2$ has an absorbance of 21.4%, and BP/MoS_2 has an absorbance of 20.2%. To sum up, we demonstrated the integrated advantages of longer electron-hole pair separation lifetime, stronger photon absorption ability and better light absorption intensity for the $BP/MoSe_2$ heterostructure, indicating a potentially excellent thin film solar-cell material.

Good absorbance is essential for the desired performance of the devices comprising atomically-thin $BP/MoSe_2$ and BP/MoS_2 in optoelectronics and photovoltaics. In Fig. 5c, both $BP/MoSe_2$ and BP/MoS_2 heterostructures exhibit excellent light absorption characteristics. We researched the practical application of $BP/MoSe_2$ heterostructure in solar cells via evaluating band edges of type-II band alignment. Furthermore, $BP/MoSe_2$ and BP/MoS_2 heterostructures form p-n junctions, in which $MoSe_2/MoS_2$ and BP serve as acceptors (n-type) and donors (p-type), respectively. As displayed in Fig. 6b, we constructed the p-n junction by combining $MoSe_2$ and BP layers. The power conversion efficiency (PCE) η can describe the ability of $BP/MoSe_2$ and BP/MoS_2

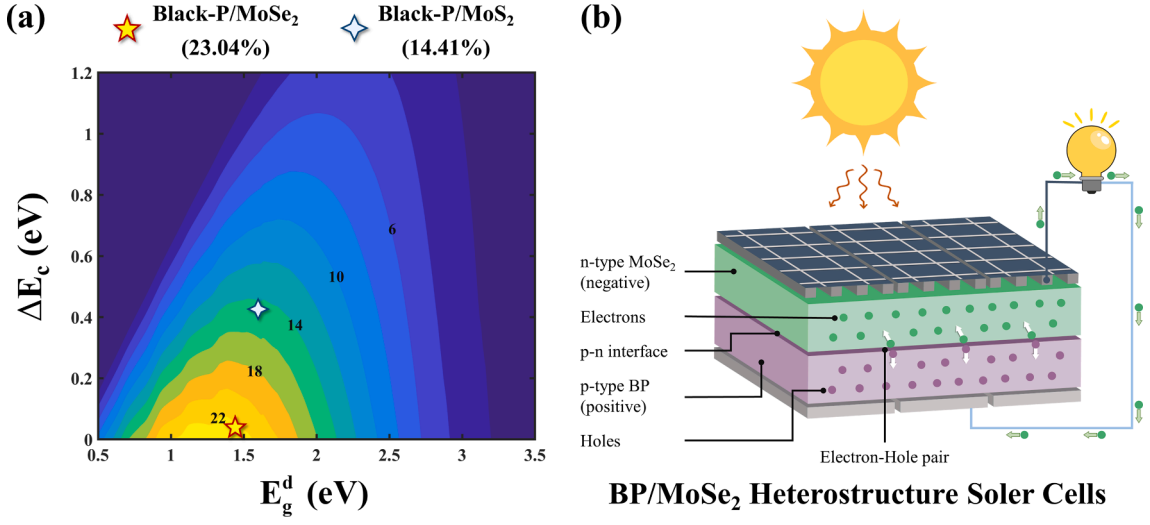

Fig. 6. (a) Calculated power conversion efficiency of $BP/MoSe_2$ and BP/MoS_2 heterostructure. (b) Operating mechanism of $BP/MoSe_2$ heterostructure in thin film solar cell.

heterostructural to convert light energy into electrical energy(Bernardi et al., 2012; Scharber et al., 2006):

$$\eta = \frac{J_{sc} V_{oc} \beta_{FF}}{P_{solar}} = \frac{0.65\left(E_g^d - \Delta E_c - 0.3\right)\int_0^{\infty} \frac{P(\hbar\omega)}{\hbar\omega} d(\hbar\omega)}{\int_{E_g^d}^{\infty} P(\hbar\omega) d(\hbar\omega)} \quad (8)$$

where $\beta_{FF} = 0.65$ is the band fill factor (Akira, 1995). E_g^d is the band-gap of the $MoSe_2/MoS_2$. ΔE_c is the is the difference between the CBM of $MoSe_2/MoS_2$ and BP. The term $(E_g^d - \Delta E_c - 0.3)$ is the maximum open-circuit voltage. $P(\hbar\omega)$ is the AM1.5 solar energy flux at photon energy $\hbar\omega$. The numerator and denominator are the short-circuit current J_{sc} limited by the 100% external quantum efficiency and the solar energy flux at AM1.5, respectively.

For the BP/$MoSe_2$ heterostructure, the CBM and VBM of $MoSe_2$ monolayer are located at −3.873 eV and −5.314 eV, respectively. The CBM of BP monolayer is at −3.868 eV, and the VBM of BP monolayer is at −4.850 eV. Obviously, the VBM and CBM of $MoSe_2$ are lower than those of BP, proving the classic type-II energy band alignment in the BP/$MoSe_2$ again. The ΔE_c between them is quite small, only 0.005 eV with a small conduction band offset, which is desirable in designing 2D excitonic solar cells. A PCE of 23.04% was calculated in BP/$MoSe_2$ heterostructure, as shown in Fig. 6a. For the BP/MoS_2 heterostructure, MoS_2 monolayer has CBM and VBM of −4.297 eV and −5.907 eV, respectively. Compared with $MoSe_2$, the difference of CBM between MoS_2 and BP is relatively large, which is 0.427 eV, as well as, the PEC is 14.41%. Compared to those reported previously, such as, BmP/MoSSe (22.97%) (Mohanta and De Sarkar, 2020), BAs/$MoSe_2$ (20.08%)(Li et al., 2021), $WS_2/MoSe_2$ (9.92%)(Vikraman et al., 2021), ψ-phosphorene/$MoSe_2$ (20.26%)(Wang et al., 2017), organic solar cells (11.70%)(Zhao et al., 2016) and so forth, the efficiency of BP/$MoSe_2$ heterostructure (23.04%) in this work is clearly competitive. Table 4 lists the PCE values of typical solar cells.

According to the previous data, after the $MoSe_2$ layer and the BP layer are built together to form a heterostructure, the $MoSe_2$ loses charge and the BP gains charge, so that an internal electric field is formed between the layers with the direction pointing from $MoSe_2$ to BP. When the BP/ $MoSe_2$ heterostructure is irradiated by sunlight, the electron-hole pairs generated at the interface are promoted by the built-in electric field, and the photogenerated electrons accelerate to flow toward the $MoSe_2$ layer, while the photogenerated holes move rapidly toward the BP layer. Conversely, in the BP/MoS_2 heterostructure, the MoS_2 accumulates charge and the BP dissipates charge. An intrinsic electric field oriented from BP to MoS_2 is formed between these layers, and this electric field prevents electrons and holes from moving toward the MoS_2 and BP layers, respectively. Therefore, BP/$MoSe_2$ has a higher PCE and is more suitable as a 2D excitonic material for solar cells, as shown in Fig. 6b. Our high solar-to-electricity energy conversion efficiency via the interfacial hybridization of $MoSe_2$ layer with BP layer will supervise the design and build of heterostructure thin film solar cells and expand its photovoltaic application.

4. Conclusion

Successfully, we developed BP/$MoSe_2$ and BP/MoS_2 heterostructures by integrating $MoSe_2/MoS_2$ layers with high-carrier-mobility black-phosphorus layer, and induced excellent power conversion efficiency of BP/$MoSe_2$ heterostructure thin film solar cell. Two heterostructures, BP/$MoSe_2$ and BP/MoS_2, have been systematically examined with regard to electronic and optical properties. Both configurations are type-II energy band arrangement. The existence of a suitable charge transfer at the interface between the BP and $MoSe_2$ layers and the resulting built-in electric field at the interface are confirmed by multiple methods. The DFT calculations show that the BP/$MoSe_2$ heterostructure exhibits excellent optical properties. It has a large dielectric constant of 13.55, a greater light absorption intensity as well as a wider absorption range.

Table 4
Related parameters and PCE in this work and references.

system	type	E_g^d (eV)	ΔE_c (eV)	PCE (%)	Ref.	Year
BP/$MoSe_2$	II	1.44	0.005	23.04	this work	2022
BP/MoS_2	II	1.61	0.427	14.41	this work	
BAs/$MoSe_2$	I	1.42	0.155	20.08	(Li et al., 2021)	2021
$WS_2/MoSe_2$				9.92	(Vikraman et al., 2021)	2021
WSe_2/ $MoSe_2$				0.12	(Najafidehaghani et al., 2021)	2021
BmP/ MoSSe	II	1.39	0.010	22.97	(Mohanta and De Sarkar, 2020)	2020
BAs/MoSSe	II	1.21	0.096	20.86	(Mohanta and De Sarkar, 2020)	
BmP/MoS_2	II	1.38	0.130	20.42	(Mohanta et al., 2020)	2020
InS/InSe	II	2.14	0.110	13.17	(Rawat et al., 2019)	2019
GP/$MoSe_2$	II	1.35	0.240	20.00	(Kaur et al., 2018)	2018
Pd_2S_3/ Pd_2Se_3	II	1.39	0.160	~20.00	(Li et al., 2018)	2018
MoS_2/ $MoSe_2$	II	1.89	0.310	~12.00	(Li et al., 2018)	2018
GeSe/SnS	II	1.64	0.230	~18.00	(Lv et al., 2018)	2018
TiNF/TiNCl	II	1.41	0.060	~22.00	(Liang et al., 2018)	2018
ψ-P/$MoSe_2$	II	1.53	0.090	20.26	(Wang et al., 2017)	2017
α-AsP/GaN	II	1.54	0.010	22.10	(Xie et al., 2016)	2016
Organic Solar Cells				11.70	(Zhao et al., 2016)	2016
MoS_2/p-Si				5.23	(Tsai et al., 2014)	2014
AA-stacked bilayer BP/MoS_2	II	0.97	0.120	~18.00	(Dai and Zeng, 2014)	2014
g-SiC_2/GaN	II	1.08	0.310	14.20	(Zhou et al., 2013)	2013

Moreover, the light transmittance is 61.1% and the absorption is 21.4% in the BP/$MoSe_2$ heterostructure. Compared with BP/MoS_2, the BP/$MoSe_2$ heterostructure has a much higher energy conversion efficiency of 23.04%, providing a more excellent photoelectric conversion performance. In conclusion, we discovered a new-type BP/$MoSe_2$ heterostructure solar cell with enhanced efficiency via deep learning of the as-constructed BP/$MoSe_2$ and BP/MoS_2 heterostructures. We found that the built-in electric field generated at the interface promotes the separation of photogenerated carriers after BP and $MoSe_2$ build up to form a heterostructure. This will drive further development of other potential 2D van der Walls heterostructures into next-generation high-specific-power thin film solar cells.

Declaration of Competing Interest

The authors declare that they have no known competing financial interests or personal relationships that could have appeared to influence the work reported in this paper.

Acknowledgement

The authors thank for the support from the Fundamental Research Funds for the Central Universities of the University of Electronic Science and Technology of China (A03018023601020), the UESTCYDRI (U04210055), the National Natural Science Foundation of China (Grants No. 12064015) and the Thousand Talents Program of Sichuan Province.

References

The AM1.5G spectrum was taken from the NREL website: http://rredc.nrel.gov/solar/spectra/am1.5 and integrated with the trapezoid rule.
A. Luque, S.H., 2011. Handbook of Photovoltaic Science and Engineering. Wiley.
Akira, F., 1995. Electrochemical measurement methods.
Baroni, S., De Gironcoli, S., Dal Corso, A., Giannozzi, P., 2001. Phonons and related crystal properties from density-functional perturbation theory. Rev. Mod. Phys. 73 (2), 515–562.

Bernardi, M., Palummo, M., Grossman, J.C., 2012. Semiconducting monolayer materials as a tunable platform for excitonic solar cells. ACS Nano 6 (11), 10082–10089.
Blöchl, P.E., 1994. Projector augmented-wave method. Phys. Rev. B 50 (24), 17953–17979.
Burschka, J., Pellet, N., Moon, S.-J., Humphry-Baker, R., Gao, P., Nazeeruddin, M.K., Grätzel, M., 2013. Sequential deposition as a route to high-performance perovskite-sensitized solar cells. Nature 499 (7458), 316–319.
Cai, Y., Zhang, G., Zhang, Y.-W., 2014. Polarity-reversed robust carrier mobility in monolayer MoS_2 nanoribbons. J. Am. Chem. Soc. 136 (17), 6269–6275.
Cakir, D., Sahin, H., Peeters, F.M., 2014. Tuning of the electronic and optical properties of single-layer black phosphorus by strain. Phys. Rev. B 90 (20).
Castellanos-Gomez, A., Poot, M., Steele, G.A., van der Zant, H.S.J., Agrait, N., Rubio-Bollinger, G., 2012. Elastic properties of freely suspended MoS_2 nanosheets. Adv. Mater. 24 (6), 772–775.
Chapin, D.M., Fuller, C.S., Pearson, G.L., 1954. A new silicon p-n junction photocell for converting solar radiation into electrical power. J. Appl. Phys. 25 (5), 676–677.
Chen, J., Zhao, X., Tan, S.J., Xu, H., Wu, B., Liu, B., Fu, D., Fu, W., Geng, D., Liu, Y., Liu, W., Tang, W., Li, L., Zhou, W., Sum, T.C., Loh, K.P., 2017. Chemical vapor deposition of large-sizemonolayer $MoSe_2$ crystals on molten glass. J. Am. Chem. Soc. 139 (3), 1073–1076.
Chen, K., Wan, X., Wen, J., Xie, W., Kang, Z., Zeng, X., Chen, H., Xu, J.-B., 2015. Electronic properties of MoS_2-WS_2 heterostructures synthesized with two-Step lateral epitaxial strategy. ACS Nano 9 (10), 9868–9876.
Chuang, H.J., Tan, X., Ghimire, N.J., Perera, M.M., Chamlagain, B., Cheng, M.M., Yan, J., Mandrus, D., Tomanek, D., Zhou, Z., 2014. High mobility WSe_2 p- and n-type field-effect transistors contacted by highly doped graphene for low-resistance contacts. Nano Lett. 14 (6), 3594–3601.
Conan, A., Bonnet, A., Zoaeter, M., Ramoul, D., 1984. Dependence of the total mobility in a one-band model applicationto n-Type $MoTe_2$. Phys. Status Solidi B 124 (1), 403–410.
D.L. Greenaway, G.H., 1968. Optical properties and band structure of semiconductors. Elsevier Ltd.
Deng, Y., Luo, Z., Conrad, N.J., Liu, H., Gong, Y., Najmaei, S., Ajayan, P.M., Lou, J., Xu, X., Ye, P.D., 2014. Black phosphorus-monolayer MoS_2 van der Waals heterojunction p-n diode. ACS Nano 8 (8), 8292–8299.
Fleurence, A., Friedlein, R., Ozaki, T., Kawai, H., Wang, Y., Yamada-Takamura, Y., 2012. Experimental evidence for epitaxial silicene on diboride thin films. Phys. Rev. Lett. 108 (24).
Gajdoš, M., Hummer, K., Kresse, G., Furthmüller, J., Bechstedt, F., 2006. Linear optical properties in the projector-augmented wave methodology. Phys. Rev. B 73 (4), 045112.
Gallagher, S.J., Norton, B., Eames, P.C., 2007. Quantum dot solar concentrators: Electrical conversion efficiencies and comparative concentrating factors of fabricated devices. Sol. Energy 81 (6), 813–821.
Ginley, D., Green, M.A., Collins, R., 2008. Solar energy conversion toward 1 terawatt. Mrs Bull. 33 (4), 355–364.
Grimme, S., 2006. Semiempirical GGA-type density functional constructed with a long-range dispersion correction. J. Comput. Chem. 27 (15), 1787–1799.
Grimme, S., Antony, J., Ehrlich, S., Krieg, H., 2010. A consistent and accurate ab initio parametrization of density functional dispersion correction (DFT-D) for the 94 elements H-Pu. J. Chem. Phys. 132 (15), 154104.
Han, Q., Bae, S.H., Sun, P., Hsieh, Y.T., Yang, Y.M., Rim, Y.S., Zhao, H., Chen, Q., Shi, W., Li, G., Yang, Y., 2016. Single crystal formamidinium lead Iodide ($FAPbI_3$): Insight into the structural, optical, and electrical properties. Adv. Mater. 28 (11), 2253–2258.
Hassan, Y., Park, J.H., Crawford, M.L., Sadhanala, A., Lee, J., Sadighian, J.C., Mosconi, E., Shivanna, R., Radicchi, E., Jeong, M., Yang, C., Choi, H., Park, S.H., Song, M.H., De Angelis, F., Wong, C.Y., Friend, R.H., Lee, B.R., Snaith, H.J., 2021. Ligand-engineered bandgap stability in mixed-halide perovskite LEDs. Nature 591 (7848), 72–77.
Henkelman, G., Arnaldsson, A., Jónsson, H., 2006. A fast and robust algorithm for Bader decomposition of charge density. Comp. Mater. Sci. 36 (3), 354–360.
Hetsch, F., Zhao, N., Kershaw, S.V., Rogach, A.L., 2013. Quantum dot field effect transistors. Mater. Today 16 (9), 312–325.
Nelson, J., 2003. The Physics of Solar Cells. Imperial College Press.
Jeong, J., Kim, M., Seo, J., Lu, H., Ahlawat, P., Mishra, A., Yang, Y., Hope, M.A., Eickemeyer, F.T., Kim, M., Yoon, Y.J., Choi, I.W., Darwich, B.P., Choi, S.J., Jo, Y., Lee, J.H., Walker, B., Zakeeruddin, S.M., Emsley, L., Rothlisberger, U., Hagfeldt, A., Kim, D.S., Gratzel, M., Kim, J.Y., 2021. Pseudo-halide anion engineering for alpha-$FAPbI_3$ perovskite solar cells. Nature 381–385.
Perdew, J.P., Burke, K., Ernzerhof, M., 1996. Generalized gradient approximation made simple. Phys. Rev. Lett. 77 (18), 3865–3868.
Kaur, S., Kumar, A., Srivastava, S., Tankeshwar, K., Pandey, R., 2018. Monolayer, bilayer, and heterostructures of green phosphorene for water splitting and photovoltaics. J. Phys. Chem. C 122 (45), 26032–26038.
Kim, G., Yeol, K., Park, M., Kim, M., Jeon, J., Song, J., Barrios-Vargas, J.E., Sato, Y., Lin, Y.-C., Suenaga, K., Roche, S., Yoo, S., Sohn, B.-H., Jeon, S., Shin, H.S., 2020. Blue emission at atomically sharp 1D heterojunctions between graphene and *h*-BN. Nat. Commun. 11 (1).
Klaassen, D.B.M., 1992. A unified mobility model for device simulation. I. Model equations and concentration dependence. Solid State Electron. 35 (7), 953–959.
Kojima, A., Teshima, K., Shirai, Y., Miyasaka, T., 2009. Organometal halide perovskites as visible-light sensitizers for photovoltaic cells. J. Am. Chem. Soc. 131 (17), 6050–6051.
Kong, J., Shin, Y., Röhr, J.A., Wang, H., Meng, J., Wu, Y., Katzenberg, A., Kim, G., Kim, D.Y., Li, T.-D., Chau, E., Antonio, F., Siboonruang, T., Kwon, S., Lee, K., Kim, J. R., Modestino, M.A., Wang, H., Taylor, A.D., 2021. CO_2 doping of organic interlayers for perovskite solar cells. Nature 594 (7861), 51–56.
Kresse, G., Furthmuller, J., 1996. Efficiency of ab-initio total energy calculations for metals and semiconductors using a plane-wave basis set. Comp. Mater. Sci. 6 (1), 15–50.
Kresse, G., Furthmüller, J., 1996. Efficient iterative schemes for *ab initio* total-energy calculations using a plane-wave basis set. Phys. Rev. B 54 (16), 11169–11186.
Kresse, G., Hafner, J., 1994. *Ab initio* molecular-dynamics simulation of the liquid-metal-amorphous-semiconductor transition in germanium. Phys. Rev. B 49 (20), 14251–14269.
Kresse, G., Joubert, D., 1999. From ultrasoft pseudopotentials to the projector augmented-wave method. Phys. Rev. B 59 (3), 1758–1775.
Larentis, S., Fallahazad, B., Tutuc, E., 2012. Field-effect transistors and intrinsic mobility in ultra-thin MoSe2 layers. Appl. Phys. Lett. 101 (22), 223104.
Lee, M.M., Teuscher, J., Miyasaka, T., Murakami, T.N., Snaith, H.J., 2012. Efficient hybrid solar cells based on meso-superstructured organometal halide perovskites. Science 338 (6107), 643–647.
Li, L., Yu, Y., Ye, G.J., Ge, Q., Ou, X., Wu, H., Feng, D., Chen, X.H., Zhang, Y., 2014. Black phosphorus field-effect transistors. Nat. Nanotechnol. 9 (5), 372–377.
Li, X., Zhang, S., Guo, Y., Wang, F.Q., Wang, Q., 2018. Physical properties and photovoltaic application of semiconducting Pd_2Se_3 monolayer. Nanomaterials 8 (10), 832.
Li, Y., Feng, Z., Sun, Q., Ma, Y., Tang, Y., Dai, X., 2021. Electronic, thermoelectric, transport and optical properties of $MoSe_2$/BAs van der Waals heterostructures. Results Phys. 23, 104010.
Liang, Y., Dai, Y., Ma, Y., Ju, L., Wei, W., Huang, B., 2018. Novel titanium nitride halide TiNX (X = F, Cl, Br) monolayers: potential materials for highly efficient excitonic solar cells. J. Mater. Chem. A 6 (5), 2073–2080.
Liechtenstein, A.I., Anisimov, V.I., Zaanen, J., 1995. Density-functional theory and strong interactions: Orbital ordering in Mott-Hubbard insulators. Phys. Rev. B 52 (8), R5467–R5470.
Liu, M., Johnston, M.B., Snaith, H.J., 2013. Efficient planar heterojunction perovskite solar cells by vapour deposition. Nature 501 (7467), 395–398.
Lv, X., Wei, W., Mu, C., Huang, B., Dai, Y., 2018. Two-dimensional GeSe for high performance thin-film solar cells. J. Mater. Chem. A 6 (12), 5032–5039.
Mak, K.F., He, K., Lee, C., Lee, G.H., Hone, J., Heinz, T.F., Shan, J., 2013. Tightly bound trions in monolayer MoS_2. Nat. Mater. 12 (3), 207–211.
Mak, K.F., He, K., Shan, J., Heinz, T.F., 2012. Control of valley polarization in monolayer MoS_2 by optical helicity. Nat. Nanotechnol. 7 (8), 494–498.
Mak, K.F., Shan, J., 2016. Photonics and optoelectronics of 2D semiconductor transition metal dichalcogenides. Nat. Photonics 10 (4), 216–226.
Mathew, X., Cruz, J.S., Coronado, D.R., Millán, A.R., Segura, G.C., Morales, E.R., Martínez, O.S., Garcia, C.C., Landa, E.P., 2012. CdS thin film post-annealing and Te-S interdiffusion in a CdTe/CdS solar cell. Sol. Energy 86 (4), 1023–1028.
Mathew, X., Enriquez, J.P., Romeo, A., Tiwari, A.N., 2004. CdTe/CdS solar cells on flexible substrates. Sol. Energy 77 (6), 831–838.
Min, H., Lee, D.Y., Kim, J., Kim, G., Lee, K.S., Kim, J., Paik, M.J., Kim, Y.K., Kim, K.S., Kim, M.G., Shin, T.J., Il Seok, S., 2021. Perovskite solar cells with atomically coherent interlayers on SnO2 electrodes. Nature 598 (7881), 444–450.
Mohanta, M.K., De Sarkar, A., 2020. Interfacial hybridization of Janus MoSSe and BX (X = P, As) monolayers for ultrathin excitonic solar cells, nanopiezotronics and low-power memory devices. Nanoscale 12 (44), 22645–22657.
Mohanta, M.K., Rawat, A., Jena, N., Dimple, Ahammed, R., De Sarkar, A., 2020. Interfacing boron monophosphide with molybdenum disulfide for an ultrahigh performance in thermoelectrics, two-dimensional excitonic solar cells, and nanopiezotronics. ACS Appl. Mater. Interfaces 12 (2), 3114–3126.
Momma, K., Izumi, F., 2008. VESTA: a three-dimensional visualization system for electronic and structural analysis. J. Appl. Crystallogr. 41 (3), 653–658.
Monkhorst, H.J., Pack, J.D., 1976. Special points for Brillouin-zone integrations. Phys. Rev. B 13 (12), 5188–5192.
Najafidehaghani, E., Gan, Z., George, A., Lehnert, T., Ngo, G.Q., Neumann, C., Bucher, T., Staude, I., Kaiser, D., Vogl, T., Hübner, U., Kaiser, U., Eilenberger, F., Turchanin, A., 2021. 1D p-n junction electronic and optoelectronic devices from transition metal dichalcogenide lateral heterostructures grown by one-pot chemical vapor deposition synthesis. Adv. Funct. Mater. 31 (27), 2101086.
Neuhauser, D., Baer, R., Rabani, E., 2014. Communication: Embedded fragment stochastic density functional theory. J. Chem. Phys. 141 (4), 041102.
Novoselov, K.S., Geim, A.K., Morozov, S.V., Jiang, D., Zhang, Y., Dubonos, S.V., Grigorieva, I.V., Firsov, A.A., 2004. Electric field effect in atomically thin carbon films. Science 306 (5696), 666–669.
Podzorov, V., Gershenson, M.E., Kloc, C., Zeis, R., Bucher, E., 2004. High-mobility field-effect transistors based on transition metal dichalcogenides. Appl. Phys. Lett. 84 (17), 3301–3303.
Polman, A., Knight, M., Garnett, E.C., Ehrler, B., Sinke, W.C., 2016. Photovoltaic materials: Present efficiencies and future challenges. Science 352 (6283), aad4424.
Qiao, J., Kong, X., Hu, Z.-X., Yang, F., Ji, W., 2014. High-mobility transport anisotropy and linear dichroism in few-layer black phosphorus. Nat. Commun. 5.
Radisavljevic, B., Radenovic, A., Brivio, J., Giacometti, V., Kis, A., 2011. Single-layer MoS_2 transistors. Nat. Nanotechnol. 6 (3), 147–150.
Rawat, A., Ahammed, R., Dimple, Jena, N., Mohanta, M.K., De Sarkar, A., 2019. Solar energy harvesting in type II van der Waals heterostructures of semiconducting group III monochalcogenide monolayers. J. Phys. Chem. C 123 (20), 12666–12675.
Rawat, A., Jena, N., Dimple, De Sarkar, A., 2018. A comprehensive study on carrier mobility and artificial photosynthetic properties in group VI B transition metal dichalcogenide monolayers. J. Mater. Chem. A 6 (18), 8693–8704.

Scharber, M.C., Mühlbacher, D., Koppe, M., Denk, P., Waldauf, C., Heeger, A.J., Brabec, C.J., 2006. Design rules for donors in bulk-heterojunction solar cells-towards 10 % energy-conversion efficiency. Adv. Mater. 18 (6), 789–794.

Shao, M.M., Shao, Y.F., Chai, J.W., Qu, Y.J., Yang, M.Y., Wang, Z.L., Yang, M., Ip, W.F., Kwok, C.T., Shi, X.Q., Lu, Z.G., Wang, S.J., Wang, X.S., Pan, H., 2017. Synergistic effect of 2D Ti_2C and g-C_3N_4 for efficient photocatalytic hydrogen production. J. Mater. Chem. A 5 (32), 16748–16756.

Shockley, W., Queisser, H.J., 1961. Detailed balance limit of efficiency of p-n junction solar cells. J. Appl. Phys. 32 (3), 510–519.

Souza, E.S., Scopel, W.L., Miwa, R.H., 2018. Probing the local interface properties at a graphene-$MoSe_2$ in-plane lateral heterostructure: an *ab initio* study. Phys. Chem. Chem. Phys. 20 (26), 17952–17960.

Stranks, S.D., Eperon, G.E., Grancini, G., Menelaou, C., Alcocer, M.J.P., Leijtens, T., Herz, L.M., Petrozza, A., Snaith, H.J., 2013. Electron-hole diffusion lengths exceeding 1 micrometer in an organometal trihalide perovskite absorber. Science 342 (6156), 341–344.

Togo, A., Tanaka, I., 2015. First principles phonon calculations in materials science. Scr. Mater. 108, 1–5.

Toll, J.S., 1956. Causality and the dispersion relation: logical foundations. Phys. Rev. 104 (6), 1760–1770.

Tsai, M.-L., Li, M.-Y., Retamal, J.R.D., Lam, K.-T., Lin, Y.-C., Suenaga, K., Chen, L.-J., Liang, G., Li, L.-J., He, J.-H., 2017. Single atomically sharp lateral monolayer p-n heterojunction solar cells with extraordinarily high power conversion efficiency. Adv. Mater. 29 (32), 1701168.

Tsai, M.-L., Su, S.-H., Chang, J.-K., Tsai, D.-S., Chen, C.-H., Wu, C.-I., Li, L.-J., Chen, L.-J., He, J.-H., 2014. Monolayer MoS_2 heterojunction solar cells. ACS Nano 8 (8), 8317–8322.

Ugeda, M.M., Bradley, A.J., Shi, S.-F., da Jornada, F.H., Zhang, Y., Qiu, D.Y., Ruan, W., Mo, S.-K., Hussain, Z., Shen, Z.-X., Wang, F., Louie, S.G., Crommie, M.F., 2014. Giant bandgap renormalization and excitonic effects in a monolayer transition metal dichalcogenide semiconductor. Nat. Mater. 13 (12), 1091–1095.

van der Marel, D., Molegraaf, H.J., Zaanen, J., Nussinov, Z., Carbone, F., Damascelli, A., Eisaki, H., Greven, M., Kes, P.H., Li, M., 2003. Quantum critical behaviour in a high-T(c) superconductor. Nature 425 (6955), 271–274.

Vikraman, D., Hussain, S., Patil, S.A., Truong, L., Arbab, A.A., Jeong, S.H., Chun, S.-H., Jung, J., Kim, H.-S., 2021. Engineering $MoSe_2/WS_2$ hybrids to replace the scarce platinum electrode for hydrogen evolution reactions and dye-sensitized solar cells. ACS Appl. Mater. Interfaces 13 (4), 5061–5072.

Wang, H., Li, X., Liu, Z., Yang, J., 2017. ψ-Phosphorene: a new allotrope of phosphorene. Phys. Chem. Chem. Phys. 19 (3), 2402–2408.

Wang, Q.H., Kalantar-Zadeh, K., Kis, A., Coleman, J.N., Strano, M.S., 2012. Electronics and optoelectronics of two-dimensional transition metal dichalcogenides. Nat. Nanotechnol. 7 (11), 699–712.

Wang, V., Xiao, W., Ma, D.-M., Liu, R.-J., Yang, C.-M., 2014. Structural, electronic, and optical properties of $GaInO_3$: A hybrid density functional study. J. Appl. Phys. 115 (4), 043708.

Wang, Z., Gutierrez-Lezama, I., Ubrig, N., Kroner, M., Gibertini, M., Taniguchi, T., Watanabe, K., Imamoglu, A., Giannini, E., Morpurgo, A.F., 2018. Very large tunneling magnetoresistance in layered magnetic semiconductor CrI_3. Nat. Commun. 9.

Wehrenfennig, C., Eperon, G.E., Johnston, M.B., Snaith, H.J., Herz, L.M., 2014. High charge carrier mobilities and lifetimes in organolead trihalide perovskites. Adv. Mater. 26 (10), 1584–1589.

Wilson, J.A., Yoffe, A.D., 1969. The transition metal dichalcogenides discussion and interpretation of the observed optical, electrical and structural properties. Adv. Phys. 18 (73), 193–335.

Wohrle, D., Meissner, D., 1991. Organic solar-cells. Adv. Mater. 3 (3), 129–138.

Wu, M.-S., Xu, B., Liu, G., Ouyang, C.-Y., 2012. The effect of strain on band structure of single-layer MoS_2: an *ab initio* study. Acta Phys. Sin-ch Ed. 61 (22).

Xie, M., Zhang, S., Cai, B., Huang, Y., Zou, Y., Guo, B., Gu, Y., Zeng, H., 2016. A promising two-dimensional solar cell donor: Black arsenic-phosphorus monolayer with 1.54 eV direct bandgap and mobility exceeding 14,000 $cm^2V^{-1}s^{-1}$. Nano Energy 28, 433–439.

Yoo, J.J., Seo, G., Chua, M.R., Park, T.G., Lu, Y., Rotermund, F., Kim, Y.-K., Moon, C.S., Jeon, N.J., Correa-Baena, J.-P., Bulovic, V., Shin, S.S., Bawendi, M.G., Seo, J., 2021. Efficient perovskite solar cells via improved carrier management. Nature 590 (7847), 587–593.

Zhao, J., Li, Y., Yang, G., Jiang, K., Lin, H., Ade, H., Ma, W., Yan, H., 2016. Efficient organic solar cells processed from hydrocarbon solvents. Nat. Energy 1 (2), 15027.

Zhou, L.-J., Zhang, Y.-F., Wu, L.-M., 2013. SiC_2 Siligraphene and nanotubes: novel donor materials in excitonic solar cells. Nano Lett. 13 (11), 5431–5436.